Wenjun Ge
School of Engineering,
University of California,
Merced, CA 95343
e-mail: wge@ucmerced.edu

Ricardo Marquez
School of Engineering,
University of California,
Merced, CA 95343
e-mail: rmarquez3@ucmerced.edu

Michael F. Modest[1]
Professor
Fellow ASME
School of Engineering,
University of California,
Merced, CA 95343
e-mail: mmodest@ucmerced.edu

Somesh P. Roy
School of Engineering,
University of California,
Merced, CA 95343
e-mail: sroy3@ucmerced.edu

Implementation of High-Order Spherical Harmonics Methods for Radiative Heat Transfer on OPENFOAM

A general formulation of the spherical harmonics (P_N) methods was developed recently to expand the method to high orders of P_N. The set of $N(N+1)/2$ three-dimensional second-order elliptic PDEs formulation and their Marshak boundary conditions for arbitrary geometries are implemented in the OPENFOAM finite volume based CFD software. The results are verified for four cases, including a 1D slab, a 2D square enclosure, a 3D cylindrical enclosure, and an axisymmetric flame. All cases have strongly varying radiative properties, and the results are compared with exact solutions and solutions from the photon Monte Carlo method (PMC). [DOI: 10.1115/1.4029546]

Keywords: radiative heat transfer, RTE solvers, spherical harmonics, computer implementation

1 Introduction

The study of radiative heat transfer in a multidimensional geometry with a strongly varying participating medium has become increasingly important in various practical applications like combustion, manufacturing, and environmental systems. The radiative transfer equation (RTE) is an integro-differential equation in five independent variables (three in space and two in direction), which is exceedingly difficult to solve. Many approximate methods have been developed over time. The most widely used approximate methods today are the discrete ordinates method (DOM) [1,2] or its finite volume version (FVM) [3], the PMC [4], and the spherical harmonics method (SHM) [5]. The DOM/FVM method discretizes the entire solid angle by finite ordinate directions and is relatively simple to implement within modern CFD software. But an iterative solution is required for scattering media or reflecting surfaces, and computational cost is high for optically thick media. The method may also suffer from ray effects and false scattering due to the angular discretization [6]. The PMC method statistically provides the exact solution with sufficient photon bundles, but accurate solutions are computationally expensive. The spherical harmonics P_N approximation is potentially more accurate than DOM/FVM at comparable computational cost, but higher order P_N are mathematically very complex and difficult to implement. The P_N method decouples spatial and directional dependencies by expanding the radiative intensity into a series of spherical harmonics. The lowest order of the P_N family, the P_1 approximation, has been extensively applied to radiative transfer problems. However, it loses accuracy when intensity is directionally very anisotropic [7], as is often the case in optically thin media. Applications of higher order SHM methods were limited to one-dimensional cases for a long time, because of the cumbersome mathematics. Recently, Modest and Yang [8,9] and Modest [10] have derived a general three-dimensional P_N formulation consisting of $N(N+1)/2$ second-order elliptic partial differential equations (PDEs) and their Marshak boundary conditions for arbitrary geometries.

The main purpose of this paper is to present the procedure of implementing high-order P_N formulations within the OPENFOAM [11] open source libraries, and a preliminary version was presented in Ref. [12]. The numerical methods used are summarized along with four example cases. The results of high-order P_N methods are found to be very close to the exact solution of the RTE and accurately predict the incident radiation and radiative heat source. Also, the time cost of the P_N methods is summarized for different examples and orders.

2 Formulation

2.1 Governing Equations. In the spherical harmonics approximation, the radiative intensity is expanded into a sum of spherical harmonics

$$I(\boldsymbol{\tau},\hat{\mathbf{s}}) = \sum_{n=0}^{N}\sum_{m=-n}^{n} I_n^m(\boldsymbol{\tau}) Y_n^m(\hat{\mathbf{s}}) \tag{1}$$

where $\boldsymbol{\tau} = \int \beta_r d\mathbf{r}$ is an optical coordinate, and β_r is the extinction coefficient. $Y_n^m(\hat{\mathbf{s}})$ are the spherical harmonics and the upper limit N is the order of the approximation. The set of $N(N+1)/2$ elliptic PDEs [10] of the P_N method for isotropic scattering in 3D Cartesian coordinates are as follows:

[1]Corresponding author.

Contributed by the Heat Transfer Division of ASME for publication in the JOURNAL OF HEAT TRANSFER. Manuscript received August 19, 2014; final manuscript received December 29, 2014; published online February 10, 2015. Assoc. Editor: Zhuomin Zhang.

For each $Y_n^m : n = 0, 2, \ldots, N-1, 0 \le m \le n$

$$\sum_{k=1}^{3}\Big\{(\mathcal{L}_{xx}-\mathcal{L}_{yy})\Big[(1+\delta_{m2})a_k^{nm}I_{n+4-2k}^{m-2}+\frac{\delta_{m1}}{2}c_k^{nm}I_{n+4-2k}^{m} + e_k^{nm}I_{n+4-2k}^{m+2}\Big] + (\mathcal{L}_{xz}+\mathcal{L}_{zx})\big[(1+\delta_{m1})b_k^{nm}I_{n+4-2k}^{m-1}+d_k^{nm}I_{n+4-2k}^{m+1}\big] + (\mathcal{L}_{xy}+\mathcal{L}_{yx})\Big[-(1-\delta_{m2})a_k^{nm}I_{n+4-2k}^{-(m-2)}+\frac{\delta_{m1}}{2}c_k^{nm}I_{n+4-2k}^{-m} + e_k^{nm}I_{n+4-2k}^{-(m+2)}\Big] + (\mathcal{L}_{yz}+\mathcal{L}_{zy}) \times\Big[-(1-\delta_{m1})b_k^{nm}I_{n+4-2k}^{-(m-1)}+d_k^{nm}I_{n+4-2k}^{-(m+1)}\Big] + (\mathcal{L}_{xx}+\mathcal{L}_{yy}-2\mathcal{L}_{zz})c_k^{nm}I_{n+4-2k}^{m}\Big\} + [\mathcal{L}_{zz}-(1-\omega\delta_{0n})]I_n^m = -(1-\omega)I_b\delta_{0n} \tag{2a}$$

and for each $Y_n^{-m} : n = 2, \ldots, N-1, 1 \le m \le n$

$$\sum_{k=1}^{3}\Big\{(\mathcal{L}_{xy}+\mathcal{L}_{yx})\Big[(1+\delta_{m2})a_k^{nm}I_{n+4-2k}^{m-2}+\frac{\delta_{m1}}{2}c_k^{nm}I_{n+4-2k}^{m} - e_k^{nm}I_{n+4-2k}^{m+2}\Big] + (\mathcal{L}_{yz}+\mathcal{L}_{zy}) \times\big[(1+\delta_{m1})b_k^{nm}I_{n+4-2k}^{m-1}-d_k^{nm}I_{n+4-2k}^{m+1}\big] + (\mathcal{L}_{xx}-\mathcal{L}_{yy})\Big[(1-\delta_{m2})a_k^{nm}I_{n+4-2k}^{-(m-2)}-\frac{\delta_{m1}}{2}c_k^{nm}I_{n+4-2k}^{-m} + e_k^{nm}I_{n+4-2k}^{-(m+2)}\Big] + (\mathcal{L}_{xz}+\mathcal{L}_{zx}) \times\Big[(1-\delta_{m1})b_k^{nm}I_{n+4-2k}^{-(m-1)}+d_k^{nm}I_{n+4-2k}^{-(m+1)}\Big] + (\mathcal{L}_{xx}+\mathcal{L}_{yy}-2\mathcal{L}_{zz})c_k^{nm}I_{n+4-2k}^{-m}\Big\} + (\mathcal{L}_{zz}-1)I_n^{-m} = 0 \tag{2b}$$

where ω is the scattering albedo, $a_k^{nm}, b_k^{nm}, c_k^{nm}, d_k^{nm}$, and e_k^{nm} are constant coefficients listed in Refs. [7] and [10], and δ_{ij} is the Kronecker delta function. The $\mathcal{L}$ operators are denoting the derivatives. For example,

$$\mathcal{L}_{xy} = \frac{1}{\beta_r}\frac{\partial}{\partial x}\left(\frac{1}{\beta_r}\frac{\partial}{\partial y}\right) \tag{3a}$$

$$\mathcal{L}_{zz} = \frac{1}{\beta_r}\frac{\partial}{\partial z}\left(\frac{1}{\beta_r}\frac{\partial}{\partial z}\right) \tag{3b}$$

2.2 Boundary Conditions. $N(N+1)/2$ boundary conditions are required and determined from general Marshak's boundary conditions [13]. However, the general Marshak's boundary conditions provide $N+1$ more equations than needed. Modest [10] recently showed that for the largest value of order N, only the even values of m should be employed for a consistent set of $N(N+1)/2$ boundary conditions

$$m = \begin{cases} -n, -n+1, \ldots, n & n = 1, 3, \ldots, N-2 \\ -n+1, -n+3, \ldots, n-1 & n = N \end{cases} \tag{4}$$

The equations for the Marshak boundary conditions for isotropic scattering are shown below, where the $\bar{Y}_n^{\pm m}$ are expressed in terms of a local coordinate system $\bar{x}, \bar{y}$ (tangential to the surface), and $\bar{z}$ (outward normal of surface).

For each $\bar{Y}_{2i-1}^0, i = 1, 2, \ldots, (N+1)/2$

$$I_w p_{0,2i-1}^0 = \sum_{l=0}^{\frac{N-1}{2}}\sum_{m'=-2l}^{2l} p_{2l,2i-1}^0\bar{\Delta}_{0,m'}^{2l}I_{2l}^{m'} + \frac{\partial}{\partial\tau_{\bar{x}}}\sum_{l=1}^{\frac{N-1}{2}}\sum_{m'=-2l}^{2l} v_{l,i}^0\bar{\Delta}_{1,m'}^{2l}I_{2l}^{m'} + \frac{\partial}{\partial\tau_{\bar{y}}}\sum_{l=1}^{\frac{N-1}{2}}\sum_{m'=-2l}^{2l} v_{l,i}^0\bar{\Delta}_{-1,m'}^{2l}I_{2l}^{m'} - \frac{\partial}{\partial\tau_{\bar{z}}}\sum_{l=0}^{\frac{N-1}{2}}\sum_{m'=-2l}^{2l} w_{l,i}^0\bar{\Delta}_{0,m'}^{2l}I_{2l}^{m'} \tag{5a}$$

and for each $\bar{Y}_{2i-1}^{\pm m}, i = 1, 2, \ldots, (N+1)/2$

$$0 = \sum_{l=0}^{\frac{N-1}{2}}\sum_{m'=-2l}^{2l} p_{2l,2i-1}^m\bar{\Delta}_{\pm m,m'}^{2l}I_{2l}^{m'} - \frac{\partial}{\partial\tau_{\bar{x}}}\sum_{l=l_1}^{\frac{N-1}{2}}\sum_{m'=-2l}^{2l}\Big[(1\pm\delta_{m,1})u_{l,i}^m\bar{\Delta}_{\pm(m-1),m'}^{2l} - v_{l,i}^m\bar{\Delta}_{\pm(m+1),m'}^{2l}\Big]I_{2l}^{m'} \pm \frac{\partial}{\partial\tau_{\bar{y}}}\sum_{l=l_2}^{\frac{N-1}{2}}\sum_{m'=-2l}^{2l}\Big[(1\mp\delta_{m,1})u_{l,i}^m\bar{\Delta}_{\mp(m-1),m'}^{2l} + v_{l,i}^m\bar{\Delta}_{\mp(m+1),m'}^{2l}\Big]I_{2l}^{m'} - \frac{\partial}{\partial\tau_{\bar{z}}}\sum_{l=0}^{\frac{N-1}{2}}\sum_{m'=-2l}^{2l} w_{l,i}^m\bar{\Delta}_{\pm m,m'}^{2l}I_{2l}^{m'} \tag{5b}$$

where l_1 and l_2 are defined as

$$l_1 = \begin{cases} 0 & \text{for } \bar{Y}_{2i-1}^m \\ 1 & \text{for } \bar{Y}_{2i-1}^{-m} \end{cases} \quad \text{and} \quad l_2 = \begin{cases} 1 & \text{for } \bar{Y}_{2i-1}^m \\ 0 & \text{for } \bar{Y}_{2i-1}^{-m} \end{cases} \tag{6}$$

I_w is the radiative intensity at wall, and the constant coefficients $u_{l,i}^m, v_{l,i}^m, w_{l,i}^m$, and $p_{2l,n}^m$ can be found in Ref. [10]. The partial derivatives in Eq. (5) are expressed in local optical coordinates as

$$\frac{\partial}{\partial\tau_{\bar{x}}} = \frac{1}{\beta_r}\frac{\partial}{\partial\bar{x}} \tag{7a}$$

$$\frac{\partial}{\partial\tau_{\bar{y}}} = \frac{1}{\beta_r}\frac{\partial}{\partial\bar{y}} \tag{7b}$$

$$\frac{\partial}{\partial\tau_{\bar{z}}} = \frac{1}{\beta_r}\frac{\partial}{\partial\bar{z}} \tag{7c}$$

The calculation of boundary conditions involves rotating local coordinates back to global coordinates through a rotation function $\bar{\Delta}(-\gamma, -\beta, -\alpha)$, which depends only on the geometry of the boundary faces. The Euler angles (α, β, γ) from the boundary faces follow the definition of Varshalovich et al. [14], see Fig. 1, and can be obtained from the surface normal $\hat{\mathbf{n}}$ of the boundary faces as

$$\begin{aligned} \alpha &= \tan^{-1}(n_y/n_x) \\ \beta &= \cos^{-1}(n_z) \\ \gamma &= \frac{\pi}{2} \end{aligned} \tag{8}$$

where n_x, n_y, and n_z are the x, y, and z components of the surface normal vector $\hat{\mathbf{n}}$, respectively. With given Euler angles, a coordinate rotation matrix $\mathbf{R}$ can be determined as

$$\mathbf{R} = \begin{bmatrix} -\sin\alpha & -\cos\alpha\cos\beta & \cos\alpha\sin\beta \\ \cos\alpha & -\sin\alpha\cos\beta & \sin\alpha\sin\beta \\ 0 & \sin\beta & \cos\beta \end{bmatrix} \tag{9}$$

allowing the evaluation of tangential directional vectors as

$$\hat{\mathbf{t}}_{\bar{x}} = \mathbf{R}\cdot\hat{\mathbf{i}} \quad \hat{\mathbf{t}}_{\bar{y}} = \mathbf{R}\cdot\hat{\mathbf{J}} \tag{10}$$

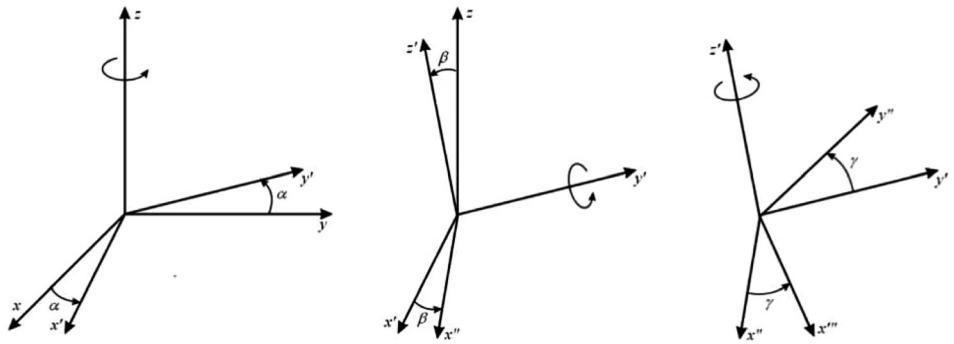

Fig. 1 Definition of Euler angles for an arbitrary rotation

3 Implementation

Generally, the system of the governing PDEs can be solved in two ways. One approach is to solve the system of equations directly by Gaussian elimination. Such direct solution does not require any iteration which will theoretically reduce the computational cost. However, Ravishankar et al. [15] point out that the size of the coefficient matrix, and the large numbers of the unknowns demand huge amounts of memory and therefore make Gaussian elimination inefficient. Another way is to adopt an iterative method, which solves one unknown at a time while holding other unknowns constant. In this paper, the coupled $N(N+1)/2$ simultaneous PDEs and their boundary conditions are solved iteratively by the finite volume based software OPENFOAM. In each PDE with n and m corresponding to $Y_n^{\pm m}$, the $I_n^{\pm m}$ and their derivatives are arranged in the finite volume Laplacian operator of OPENFOAM, i.e.,

$$(\mathcal{L}_{xx}+\mathcal{L}_{yy}-2\mathcal{L}_{zz})c_2^{nm}I_n^{\pm m}+\mathcal{L}_{zz}I_n^{\pm m}-(1-\omega\delta_{0n})I_n^{\pm m} = c_2^{nm}\nabla_\tau^2 I_n^{\pm m}+(1-3c_2^{nm})\mathcal{L}_{zz}I_n^{\pm m}-(1-\omega\delta_{0n})I_n^{\pm m} \quad (11)$$

All terms other than $I_n^{\pm m}$ are updated before each $Y_n^{\pm m}$ iteration. The preconditioned conjugate gradient (PCG) [16] algorithm is used to solve each PDE sequentially until I_0^0 is converged to prescribed criteria.

Since the governing equations are solved iteratively, the boundary conditions expressed in Eq. (5) cannot be directly implemented. In this paper, a matrix formulation is implemented so that individual Robin boundary conditions can be explicitly associated with each governing equation as

$$I_n^m+k\frac{\partial I_n^m}{\partial\tau_{\bar{z}}}=f\left(\frac{\partial I_n^m}{\partial\tau_{\bar{x}}},\frac{\partial I_n^m}{\partial\tau_{\bar{y}}},\frac{\partial I_{n'}^{m'}}{\partial\tau_{\bar{x}}},\frac{\partial I_{n'}^{m'}}{\partial\tau_{\bar{y}}},\frac{\partial I_{n'}^{m'}}{\partial\tau_{\bar{z}}}\right) \quad (12)$$

where k is a scalar constant and f is a function of partial derivatives of other intensity coefficients, including the tangential derivatives of I_n^m. Such formulations can be efficiently obtained by first expressing the system of $N(N+1)/2$ boundary conditions in matrix form, and then transforming the matrices to generate one Robin-type boundary condition for each corresponding governing equation.

We will here take the boundary conditions of the P_3 approximation as a demonstration to show the construction of coefficient matrices. The associated local spherical harmonics for P_3 are $\bar{Y}_1^0,\bar{Y}_3^0,\bar{Y}_1^{-1},\bar{Y}_1^1,\bar{Y}_3^{-2}$, and $\bar{Y}_3^2$. The coefficients in front of I_n^m and their derivatives for each boundary conditions are determined from m and n pairs of the local spherical harmonics.

The first term on the right-hand side of boundary conditions (5*a*) for equation of $\bar{Y}_1^0$ $(n=1, m=0)$ is

$$\sum_{l=0}^{\frac{N-1}{2}}\sum_{m'=-2l}^{2l}p_{2l,1}^0\bar{\Delta}_{0,m'}^{2l}I_{2l}^{m'} = \left[p_{0,1}^0\bar{\Delta}_{0,0}^0,p_{2,1}^0\bar{\Delta}_{0,-2}^2,p_{2,1}^0\bar{\Delta}_{0,-1}^2,p_{2,1}^0\bar{\Delta}_{0,0}^2,p_{2,1}^0\bar{\Delta}_{0,1}^2,p_{2,1}^0\bar{\Delta}_{0,2}^2\right]\cdot\mathbf{I} = \mathbf{q}_{(1,0)}\cdot\mathbf{I} \quad (13)$$

the subscripts of $\mathbf{q}_{(n,m)}$ show the n and m associated with $\bar{Y}_n^m$, and the vector $\mathbf{I}$ is defined as

$$\mathbf{I}=\begin{bmatrix}I_0^0\\I_2^{-2}\\I_2^{-1}\\I_2^0\\I_2^1\\I_2^2\end{bmatrix}=\begin{bmatrix}I_1\\I_2\\I_3\\I_4\\I_5\\I_6\end{bmatrix} \quad (14)$$

Applying the same formulation to the rest of the equations associated with the remaining $\bar{Y}_n^m$, the coefficients in front of I_n^m for the entire system of equations may be expressed as

$$\mathbf{Q}=\begin{bmatrix}\mathbf{q}_{(1,0)}\\\mathbf{q}_{(3,0)}\\\mathbf{q}_{(1,-1)}\\\mathbf{q}_{(1,1)}\\\mathbf{q}_{(3,-2)}\\\mathbf{q}_{(3,2)}\end{bmatrix} = \begin{bmatrix} p_{0,1}^0\bar{\Delta}_{0,0}^0 & p_{2,1}^0\bar{\Delta}_{0,-2}^2 & p_{2,1}^0\bar{\Delta}_{0,-1}^2 & p_{2,1}^0\bar{\Delta}_{0,0}^2 & p_{2,1}^0\bar{\Delta}_{0,1}^2 & p_{2,1}^0\bar{\Delta}_{0,2}^2\\ p_{0,3}^0\bar{\Delta}_{0,0}^0 & p_{2,3}^0\bar{\Delta}_{0,-2}^2 & p_{2,3}^0\bar{\Delta}_{0,-1}^2 & p_{2,3}^0\bar{\Delta}_{0,0}^2 & p_{2,3}^0\bar{\Delta}_{0,1}^2 & p_{2,3}^0\bar{\Delta}_{0,2}^2\\ 0 & p_{2,1}^1\bar{\Delta}_{-1,-2}^2 & p_{2,1}^1\bar{\Delta}_{-1,-1}^2 & p_{2,1}^1\bar{\Delta}_{-1,0}^2 & p_{2,1}^1\bar{\Delta}_{-1,1}^2 & p_{2,1}^1\bar{\Delta}_{-1,2}^2\\ 0 & p_{2,1}^1\bar{\Delta}_{1,-2}^2 & p_{2,1}^1\bar{\Delta}_{1,-1}^2 & p_{2,1}^1\bar{\Delta}_{1,0}^2 & p_{2,1}^1\bar{\Delta}_{1,1}^2 & p_{2,1}^1\bar{\Delta}_{1,2}^2\\ 0 & p_{2,3}^2\bar{\Delta}_{-2,-2}^2 & p_{2,3}^2\bar{\Delta}_{-2,-1}^2 & p_{2,3}^2\bar{\Delta}_{-2,0}^2 & p_{2,3}^2\bar{\Delta}_{-2,1}^2 & p_{2,3}^2\bar{\Delta}_{-2,2}^2\\ 0 & p_{2,3}^2\bar{\Delta}_{2,-2}^2 & p_{2,3}^2\bar{\Delta}_{2,-1}^2 & p_{2,3}^2\bar{\Delta}_{2,0}^2 & p_{2,3}^2\bar{\Delta}_{2,1}^2 & p_{2,3}^2\bar{\Delta}_{2,2}^2\end{bmatrix} \quad (15)$$

Let $\mathbf{Q}_{\bar{x}},\mathbf{Q}_{\bar{y}}$, and $\mathbf{Q}_{\bar{z}}$ be the coefficient matrices for $\partial\mathbf{I}/\partial\tau_{\bar{x}}$, $\partial\mathbf{I}/\partial\tau_{\bar{y}}$, and $\partial\mathbf{I}/\partial\tau_{\bar{z}}$, respectively. The resulting form for the $\mathbf{Q}_{\bar{x}}$ matrix is shown here:

$$\mathbf{Q}_{\bar{x}} = \begin{bmatrix} \mathbf{q}_{\bar{x}(1,0)} \\ \mathbf{q}_{\bar{x}(3,0)} \\ \mathbf{q}_{\bar{x}(1,-1)} \\ \mathbf{q}_{\bar{x}(1,1)} \\ \mathbf{q}_{\bar{x}(3,-2)} \\ \mathbf{q}_{\bar{x}(3,2)} \end{bmatrix}$$

$$= \begin{bmatrix} 0 & v^0_{1,1}\bar{\Delta}^2_{1,-2} & v^0_{1,1}\bar{\Delta}^2_{1,-1} & \cdots & v^0_{1,1}\bar{\Delta}^2_{1,2} \\ 0 & v^0_{1,2}\bar{\Delta}^2_{1,-2} & v^0_{1,2}\bar{\Delta}^2_{1,-1} & \cdots & v^0_{1,2}\bar{\Delta}^2_{1,2} \\ 0 & v^1_{1,1}\bar{\Delta}^2_{-2,-2} & v^1_{1,1}\bar{\Delta}^2_{-1,-1} & \cdots & v^1_{1,1}\bar{\Delta}^2_{-2,2} \\ v^1_{0,1}\bar{\Delta}^0_{2,0} & v^1_{1,1}\bar{\Delta}^2_{2,-2} & v^1_{1,1}\bar{\Delta}^2_{2,-1} & \cdots & v^1_{1,1}\bar{\Delta}^2_{2,2} \\ 0 & v^2_{1,2}\bar{\Delta}^2_{2,-2} & v^2_{1,2}\bar{\Delta}^2_{2,-1} & \cdots & v^2_{1,2}\bar{\Delta}^2_{2,2} \\ v^2_{0,2}\bar{\Delta}^0_{3,0} & v^2_{1,2}\bar{\Delta}^2_{3,-2} & v^2_{1,2}\bar{\Delta}^2_{3,-1} & \cdots & v^2_{1,2}\bar{\Delta}^2_{3,2} \end{bmatrix}$$

$$- \begin{bmatrix} 0 & 0 & 0 & \cdots & 0 \\ 0 & 0 & 0 & \cdots & 0 \\ 0 & 0 & 0 & \cdots & 0 \\ 2u^1_{0,1}\bar{\Delta}^0_{0,0} & 2u^1_{1,1}\bar{\Delta}^2_{0,-2} & 2u^1_{1,1}\bar{\Delta}^2_{0,-1} & \cdots & 2u^1_{1,1}\bar{\Delta}^2_{0,2} \\ 0 & 2u^2_{1,2}\bar{\Delta}^2_{-1,-2} & 2u^2_{1,2}\bar{\Delta}^2_{-1,-1} & \cdots & 2u^2_{1,2}\bar{\Delta}^2_{-1,2} \\ u^2_{0,2}\bar{\Delta}^0_{1,0} & u^2_{1,2}\bar{\Delta}^2_{1,-2} & u^2_{1,2}\bar{\Delta}^2_{1,-1} & \cdots & u^2_{1,2}\bar{\Delta}^2_{1,2} \end{bmatrix} \tag{16}$$

Finally, let $\mathbf{p}$ be the coefficient vector for I_w on the left-hand side of Eq. (5*a*), which only has a nonzero value when $m=0$

$$\mathbf{p} = \begin{bmatrix} p_{(1,0)} \\ p_{(3,0)} \\ p_{(1,-1)} \\ p_{(1,1)} \\ p_{(3,-2)} \\ p_{(3,2)} \end{bmatrix} = \begin{bmatrix} p^0_{0,1} \\ p^0_{0,3} \\ 0 \\ 0 \\ 0 \\ 0 \end{bmatrix} \tag{17}$$

Two observations regarding the above matrices may be made. First, all coefficient matrices are functions of geometry only, and thus they only need to be calculated once. The second is that the first column of matrix $\mathbf{Q}$ and vector $\mathbf{p}$ is identical, which leads to

$$\mathbf{Q}^{-1} \cdot \mathbf{p} = [1,0,0,0,0,0]^{\mathrm{T}} \tag{18}$$

which will be employed later in this section.

For general orders of P_N, the row vectors of the boundary condition are given by

$$\mathbf{q}_{(n,\pm m)} = \left[\delta_{m,0}p^m_{0,n}, p^m_{2,n}\bar{\Delta}^2_{\pm m,-2}, p^m_{2,n}\bar{\Delta}^2_{\pm m,-1}, \ldots, p^m_{2,n}\bar{\Delta}^2_{\pm m,2}, p^m_{4,n}\bar{\Delta}^4_{\pm m,-4}, \ldots, p^m_{N-1,n}\bar{\Delta}^{N-1}_{\pm m,N-1}\right] \tag{19a}$$

$$\mathbf{q}_{\bar{x}(n,0)} = \left[0, v^0_{1,i}\bar{\Delta}^2_{1,-2}, v^0_{1,i}\bar{\Delta}^2_{1,-1}, \ldots, v^0_{1,i}\bar{\Delta}^2_{1,2}, \ldots, v^0_{((N-1)/2),i}\bar{\Delta}^{N-1}_{1,N-1}\right] \tag{19b}$$

$$\mathbf{q}_{\bar{x}(n,-m)} = \left[0, v^m_{1,i}\bar{\Delta}^2_{-(m+1),-2}, v^m_{1,i}\bar{\Delta}^2_{-(m+1),-1}, \ldots, v^m_{1,i}\bar{\Delta}^2_{-(m+1),2}, \ldots, v^m_{((N-1)/2),i}\bar{\Delta}^{N-1}_{-(m+1),N-1}\right] - (1-\delta_{m,1}) \times \left[0, u^m_{1,i}\bar{\Delta}^2_{-(m-1),-2}, u^m_{1,i}\bar{\Delta}^2_{-(m-1),-1}, \ldots, u^m_{1,i}\bar{\Delta}^2_{-(m-1),2}, \ldots, u^m_{((N-1)/2),i}\bar{\Delta}^{N-1}_{-(m-1),N-1}\right] \tag{19c}$$

$$\mathbf{q}_{\bar{x}(n,+m)} = \left[v^m_{0,i}\bar{\Delta}^0_{m+1,0}, v^m_{1,i}\bar{\Delta}^2_{m+1,-2}, v^m_{1,i}\bar{\Delta}^2_{m+1,-1}, \ldots, v^m_{1,i}\bar{\Delta}^2_{m+1,2}, \ldots, v^m_{((N-1)/2),i}\bar{\Delta}^{N-1}_{m+1,N-1}\right] - (1+\delta_{m,1}) \times \left[u^m_{0,i}\bar{\Delta}^0_{m-1,0}, u^m_{1,i}\bar{\Delta}^2_{m-1,-2}, u^m_{1,i}\bar{\Delta}^2_{m-1,-1}, \ldots, u^m_{1,i}\bar{\Delta}^2_{m-1,2}, \ldots, u^m_{((N-1)/2),i}\bar{\Delta}^{N-1}_{m-1,N-1}\right] \tag{19d}$$

$$\mathbf{q}_{\bar{y}(n,0)} = \left[0, v^0_{1,i}\bar{\Delta}^2_{-1,-2}, v^0_{1i}\bar{\Delta}^2_{-1,-1}, \ldots, v^0_{1,i}\bar{\Delta}^2_{-1,2}, \ldots, v^0_{((N-1)/2),i}\bar{\Delta}^{N-1}_{-1,N-1}\right] \tag{19e}$$

$$\mathbf{q}_{\bar{y}(n,-m)} = -\left[v^m_{0,i}\bar{\Delta}^0_{m+1,0}, v^m_{1i}\bar{\Delta}^2_{m+1,-2}, v^m_{1,i}\bar{\Delta}^2_{m+1,-1}, \ldots, v^m_{1,i}\bar{\Delta}^2_{m+1,2}, \ldots, v^m_{((N-1)/2),i}\bar{\Delta}^{N-1}_{m+1,N-1}\right] - (1+\delta_{m,0}) \times \left[u^m_{0,i}\bar{\Delta}^0_{m-1,0}, u^m_{1,i}\bar{\Delta}^2_{m-1,-2}, u^m_{1,i}\bar{\Delta}^2_{m-1,-1}, \ldots, u^m_{1,i}\bar{\Delta}^2_{m-1,2} \ldots, u^m_{((N-1)/2),i}\bar{\Delta}^{N-1}_{m-1,N-1}\right] \tag{19f}$$

$$\mathbf{q}_{\bar{y}(n,+m)} = \left[0, v^m_{1,i}\bar{\Delta}^2_{-(m+1),-2}, v^m_{1,i}\bar{\Delta}^2_{-(m+1),-1}, \ldots, v^m_{1,i}\bar{\Delta}^2_{-(m+1),2}, \ldots, v^m_{((N-1)/2),i}\bar{\Delta}^{N-1}_{-(m+1),N-1}\right] + (1-\delta_{m,1}) \times \left[0, u^m_{1,i}\bar{\Delta}^2_{-(m-1),-2}, u^m_{1,i}\bar{\Delta}^2_{-(m-1),-1}, \ldots, u^m_{1,i}\bar{\Delta}^2_{-(m-1),2}, \ldots, u^m_{((N-1)/2),i}\bar{\Delta}^{N-1}_{-(m-1),N-1}\right] \tag{19g}$$

$$\mathbf{q}_{\bar{z}(n,\pm m)} = -\left[\delta_{m,0}w^m_{0,n}, w^m_{2,n}\bar{\Delta}^2_{\pm m,-2}, w^m_{2,n}\bar{\Delta}^2_{\pm m,-1}, \ldots, w^m_{2,n}\bar{\Delta}^2_{\pm m,2}, w^m_{4,n}\bar{\Delta}^4_{\pm m,-4}, , \ldots, w^m_{N-1,n}\bar{\Delta}^{N-1}_{\pm m,N-1}\right] \tag{19h}$$

where the case of $m=0$ is included in the $\pm m$ notation for Eq. (19*a*), while for the rest, the $m=0$ case is shown separately for clarity.

The entire set of boundary equations (5) for general P_N boundary conditions may now be written in matrix form as

$$\mathbf{Q} \cdot \mathbf{I} + \mathbf{Q}_{\bar{x}} \cdot \frac{\partial \mathbf{I}}{\partial \tau_{\bar{x}}} + \mathbf{Q}_{\bar{y}} \cdot \frac{\partial \mathbf{I}}{\partial \tau_{\bar{y}}} + \mathbf{Q}_{\bar{z}} \cdot \frac{\partial \mathbf{I}}{\partial \tau_{\bar{z}}} = I_w \mathbf{p} \tag{20}$$

After all elements of the coefficient matrices are calculated, the next step is to convert Eq. (20) into individual Robin-type boundary conditions, Eq. (12), which can then be directly applied to each corresponding governing equation. Let j be the row index of the matrices, as given by Eq. (14), the $(N+1)N/2$ Robin boundary conditions are

$$I_j + Z_{j,j}\frac{\partial I_j}{\partial \tau_{\bar{z}}} = \delta_{j,1}I_w - \sum_{k=1}^{N_2}\left[X_{j,k}\frac{\partial I_k}{\partial \tau_{\bar{x}}} + Y_{j,k}\frac{\partial I_k}{\partial \tau_{\bar{y}}} + (1-\delta_{j,k})Z_{j,k}\frac{\partial I_k}{\partial \tau_{\bar{z}}}\right] \tag{21}$$

where

$$\begin{aligned} \mathbf{X} &= \mathbf{Q}^{-1} \cdot \mathbf{Q}_{\bar{\mathbf{x}}} \\ \mathbf{Y} &= \mathbf{Q}^{-1} \cdot \mathbf{Q}_{\bar{\mathbf{y}}} \\ \mathbf{Z} &= \mathbf{Q}^{-1} \cdot \mathbf{Q}_{\bar{\mathbf{z}}} \end{aligned} \tag{22}$$

The coefficient matrix for the normal derivative $\partial \mathbf{I}/\partial \tau_{\bar{z}}$ is split into two parts. The diagonal elements of $\mathbf{Z}$ are kept on the left-hand side, and the rest are placed on the right-hand side. In order to calculate $\mathbf{X}$, $\mathbf{Y}$, and $\mathbf{Z}$, LU decomposition [17] of $\mathbf{Q}$ is

employed. Usually, the governing equation of I_0^0 is the first one to be solved, so it is convenient to let I_1 be I_0^0. Equation (18) is readily shown to be valid for arbitrary orders of P_N, and thus the coefficient in front of I_w in Eq. (21) is 1 when $j=1$ and equals 0 for all other cases.

For Robin-type boundary conditions, OPENFOAM calculates the value of the dependent variable at the patch faces as

$$I_{j,\text{face}} = f \times \text{RHS} + (1-f) I_{j,\text{center}} \tag{23}$$

where RHS is the right-hand side of Eq. (21), The fraction f is

$$f = \left(1 - \frac{Z_{j,j}}{\beta_r \delta}\right)^{-1} \tag{24}$$

where δ is the distance between face center and neighboring cell center. The sign before $Z_{j,j}$ in Eq. (24) differs from that in OPENFOAM, because the definition of normal direction in OPENFOAM is outward, which is the opposite to the normal direction in the P_N formulation (inward). Also, OPENFOAM discretizes the gradient term on the left-hand side of Eq. (21) as

$$\frac{\partial I}{\partial \bar{z}} = \frac{I_{\text{face}} - I_{\text{center}}}{\delta} \tag{25}$$

When the extinction coefficient β_r near the boundary is small, a stabilizer for the Robin-type boundary conditions is applied, by adding a factor of λI_i to both sides followed by division of the whole equation by $(1+\lambda)$, where $\lambda = c/\beta$, and c is a constant and has dimensions of 1/length, so that λ is dimensionless. This can help to deal with sharp gradients at the boundaries and avoid unphysical negative I_0^0 during the iterations. Therefore,

$$\begin{aligned} I_j + \left(\frac{1}{1+\lambda}\right) Z_{j,j} \frac{\partial I_j}{\partial \tau_{\bar{z}}} = {} & \left(\frac{1}{1+\lambda}\right) I_w p_j \delta_{j,1} \\ & - \left(\frac{1}{1+\lambda}\right) \sum_{k=1}^{N} \left[X_{j,k} \frac{\partial I_k}{\partial \tau_{\bar{x}}} + Y_{j,k} \frac{\partial I_k}{\partial \tau_{\bar{y}}} \right. \\ & \left. + (1-\delta_{j,k}) Z_{j,k} \frac{\partial I_k}{\partial \tau_{\bar{z}}} \right] + \left(\frac{\lambda}{1+\lambda}\right) I_j \end{aligned} \tag{26}$$

and f becomes

$$f = \left(1 - \frac{Z_{j,j}}{(1+\lambda)\beta_r \delta}\right)^{-1} \tag{27}$$

4 Results and Discussion

Four example problems are tested to explore the accuracy and computation efficiency of high-order P_N methods for fields with strongly varying temperatures and absorption coefficients. Although isotropic scattering adds no additional complexity or effort to P_N (as opposite to DOM), all the examples are limited to nonscattering media in this study simply to reduce parameters needed for presentation. For the first three examples, all quantities (Planck function, lengths, and absorption coefficient) are given in nondimensional form; in the last example, actual dimensions pertaining to the chosen flame are used.

4.1 1D Slab With Variable Medium Properties. In the first verification example, the P_N-approximations are applied to a 1D slab that encloses a medium with variable properties. In the OPENFOAM finite volume implementation, a 1D slab case may be solved by treating walls at two suppressed dimensions (single cell in these directions) of a 3D cube as perfectly reflective (symmetry boundary). The symmetry boundary in OPENFOAM sets the normal gradient at the wall to zero for scalars. While this is not true for all I_n^m terms in general, it is the case for all nonzero I_n^m terms in a one-dimensional problem and, thus, is employed here. Here, a $100 \times 1 \times 1$ cube is employed.

The properties of the medium vary according to

$$I_b = 10(1 + 0.5r^2) \tag{28a}$$

$$\kappa = r \tag{28b}$$

where r is the perpendicular distance from the lower wall. For this problem, the walls of the enclosure are assumed cold and black, and the thickness of the slab is $L=1$, and the optical thickness is $\tau_L = 1/2$. In optical coordinates, the temperature field (I_b) is linear, which is convenient for finding an analytical solution. For the numerical computations, a lower limit of $\kappa_{\min} = 10^{-4}$ was set for κ in order to avoid division by 0 at the lower wall. Although this example is only 1D, having the analytical solutions is useful for purposes of verifying certain aspects of the P_N approximation and the program implementation itself. For instance, by orienting the 1D slab at different angles within each of the three coordinate planes (see Fig. 2), the 1D slab can be used to verify that all partial derivatives are accounted for correctly in the implementation. For example, setting the configuration angle to $\phi = 0$ with the slab positioned in the x-y plane, one can test the $\mathcal{L}_{xx}$ derivatives, neglecting all mixed derivative, $\mathcal{L}_{yy}$, and $\mathcal{L}_{zz}$ terms from the PDEs. Similarly, setting $\phi = 90$ deg, the combination of $\mathcal{L}_{yy}$ derivatives can be singled out, and for $\phi = 45$ deg, the combination of $\mathcal{L}_{xx}, \mathcal{L}_{yy}, \mathcal{L}_{xy}$, and $\mathcal{L}_{yx}$ terms can be verified, etc. In terms of solution profiles within the slab, the solutions for I_0^0 should be identical (and matching the analytical profiles) for arbitrary orientations of the 1D slab.

The numerical and analytical solution for incident radiation G and divergence of flux $-\nabla \cdot \mathbf{q}$, for the case of the slab oriented in the y-direction is shown in Fig. 3. The numerical results are found to perfectly overlap the analytical results for various orientations, which demonstrate that the P_N implementation correctly employs

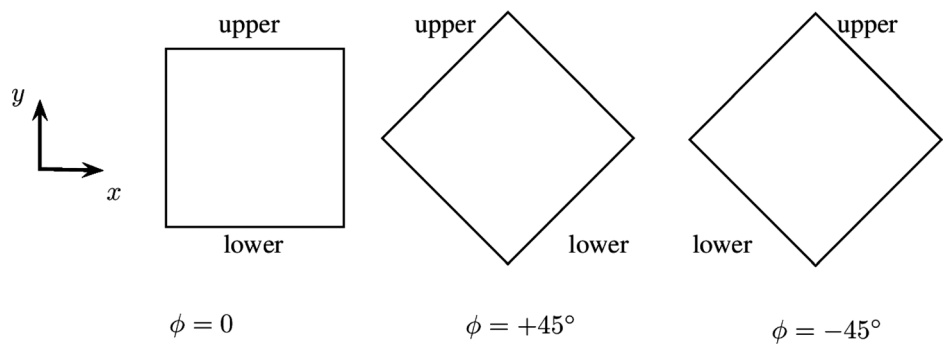

Fig. 2 Rotations of 1D slab at angles $\phi = 0, 45$ deg, -45 deg in the x-y plane. The medium properties increase with low values at the lower wall to higher values at the upper wall.

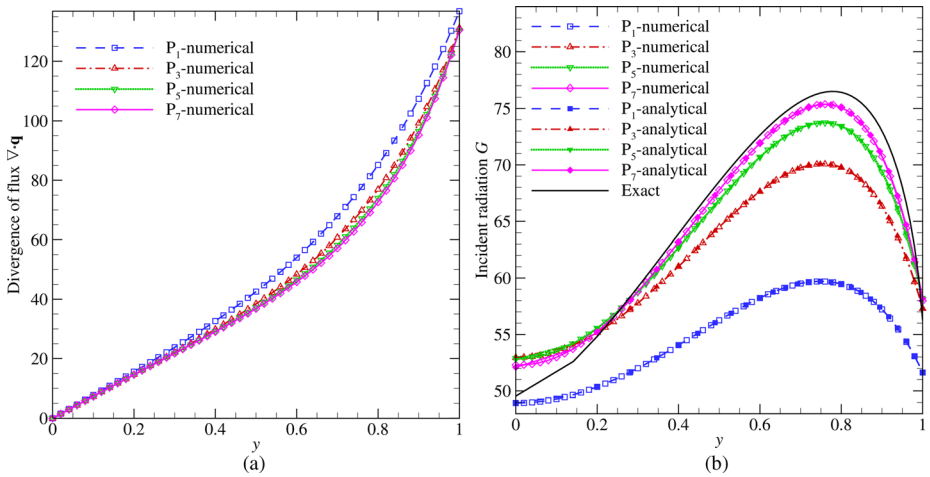

Fig. 3 Comparing incident radiation and radiative heat source with analytical solutions of P_N and exact solution of 1D slab. (*a*) Incident radiation G and (*b*) radiative heat source $\nabla \cdot \mathbf{q}$.

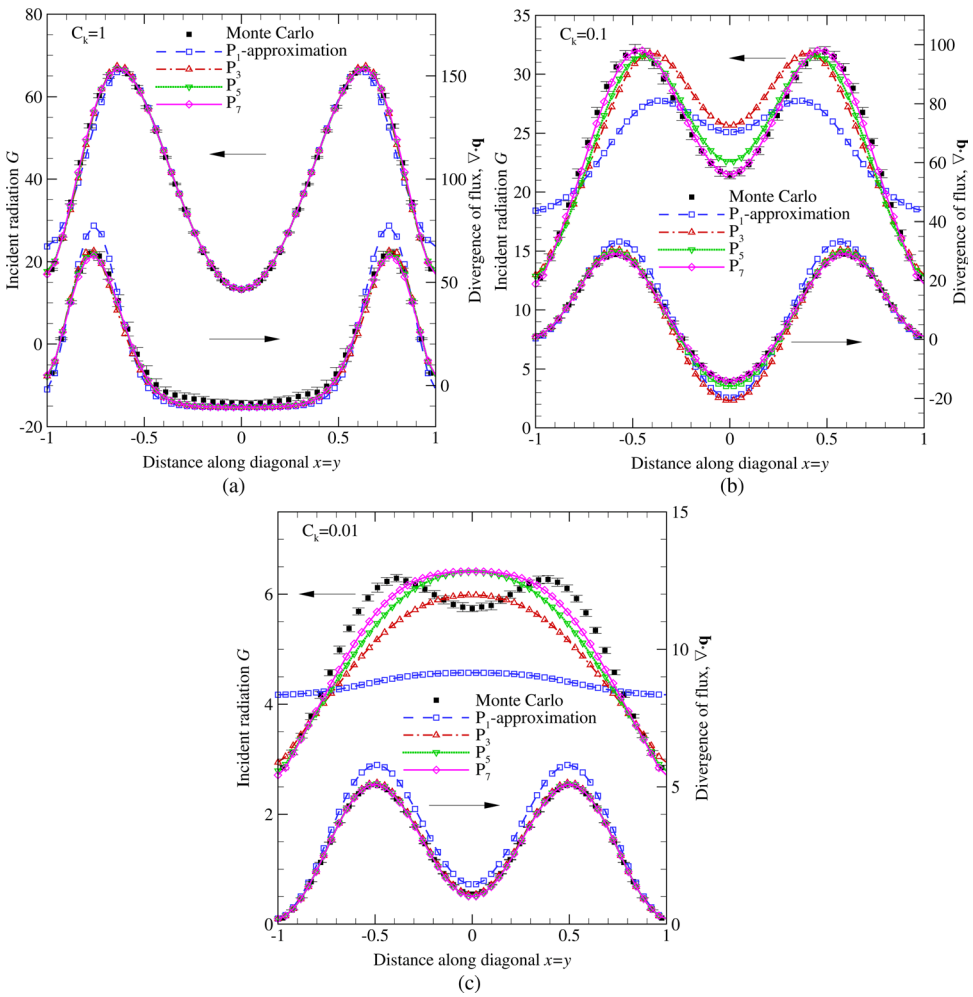

Fig. 4 Incident radiation and radiative source for a square enclosure with various P_N approximations. (*a*) $C_k = 1$, (*b*) $C_k = 0.1$, and (*c*) $C_k = 0.01$.

all the terms in the PDEs. Comparing with the exact solution for this 1D problem [7], higher order P_N generally produce more accurate results over the entire slab, except near the lower wall where it seems that the P_N-approximations incur larger errors. This is probably due to very low values of κ at the lower wall. Nevertheless, the overall error is reduced by approximately 50% every time the order is increased for this example.

4.2 Square Enclosure With Variable Radiative Properties. A verification case of a square enclosure is tested with strongly

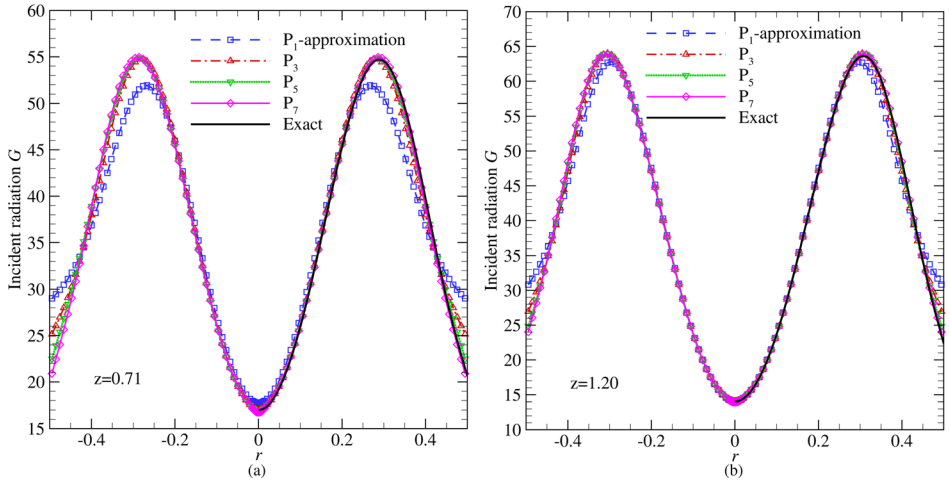

Fig. 5 Incident radiation for a cylinder enclosure at two axial locations with various P_N approximations. (*a*) $z = 0.71$ and (*b*) $z = 1.20$.

varying temperatures and absorption coefficients. Like the 1D slab case, the 2D square case is solved by treating the walls of a 3D cubic at one suppressed dimension as perfectly reflective (symmetry boundary). The square uses a $51 \times 51 \times 1$ mesh, and the boundaries are assumed black and cold.

The following nondimensional radiative properties were chosen identical to the example given in Ref. [10], and some results are shown in Fig. 4:

$$I_b = 1 + 5r^2(2 - r^2) \tag{29a}$$

$$\kappa = C_k\left[1 + 3.75(2 - r^2)^2\right] \tag{29b}$$

$$r^2 = x^2 + y^2, \quad -1 \le x \le 1, \ -1 \le y \le 1 \tag{29c}$$

$$\tau_D = 18\sqrt{2}C_k \tag{29d}$$

Comparing results from the P_N methods with a Monte Carlo simulation for the optically thick case, Figs. 4(*a*) shows that all orders of SHMs do very well. For the optically intermediate case, Fig. 4(*b*), P_1 and P_3 have difficulty catching the trend of peaks and valleys for the incident radiation G, while P_5 is very close to the PMC results and P_7 is almost exact. For the optically thin case, Fig. 4(*c*), higher orders of P_N will have better accuracy, but none can follow the true variation of incident radiation G. However, the more important radiative heat source $-\nabla \cdot \mathbf{q}$ is captured well even for optically thin situations. The placement of the 2D square enclosure to different coordinate planes (x-y, x-z, y-z) gives identical results for I_0^0 and G, while the other I_n^m terms change with different coordinate orientations.

4.3 Cylindrical Enclosure With Variable Radiative Properties. A cylindrical enclosure with variable radiative properties is tested with the P_N methods. The absorption coefficient κ varies both in the r-direction and z-directions. The cylinder has 45 cells along the radius and 40 cells along the axis with a square cuboid ($15 \times 15 \times 40$) at the center, and the cylinder walls are again set to be black and cold. The radiative properties and geometry information are

$$I_b = 1 + \frac{20}{R^4}r^2(R^2 - r^2) \tag{30a}$$

$$\kappa = C_k\left[1 + \frac{15}{R^4}(R^2 - r^2)^2\right] \tag{30b}$$

$$C_k = 0.3 + z \quad 0 \le r \le R = 0.5, \ 0 \le z \le 2.5 \tag{30c}$$

$$\tau_D = 2\int_0^R \kappa dr = 7.5C_k \tag{30d}$$

The results are shown in Fig. 5. Incident radiation G at two heights z is plotted, and the results are compared with the exact solution [7]. The results from P_3 to P_7 are very close to the exact solution, while P_1 has certain levels of discrepancies with the exact solution and the discrepancy decreases with increasing optical thickness. The incident radiation G from P_5 and P_7 correctly catch the sharp gradient near the cylinder wall, which is critical for the heat transfer analysis for some industrial applications.

While this problem is 2D axisymmetric in r and z, the P_N formulation is in Cartesian coordinates and must be solved in 3D (as is also the case for the discrete ordinates finite volume method [7]). An axisymmetric version of the P_N formulation will be presented in a follow-up paper.

4.4 Scaled Flame With Nongray Radiative Properties. Finally, the P_N implementation is applied to an axisymmetric methane jet flame. The flame is a four-time scaled 3D cylindrical version of Sandia Flame D [18]. The flame is mapped to a 3D cylinder from the original wedge mesh used by OPENFOAM for axisymmetric problems. The cylinder has 27 cells along the radius

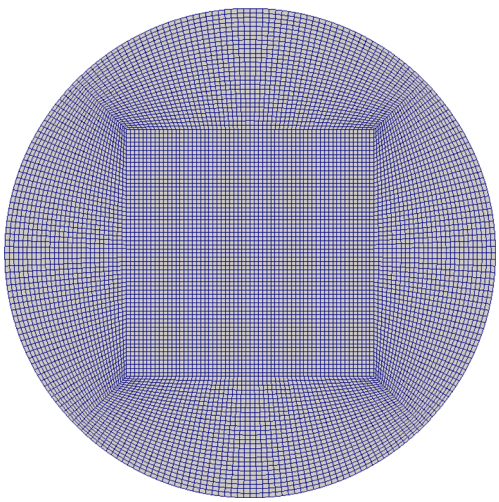

Fig. 6 Cylinder mesh of scaled Flame D in the analysis

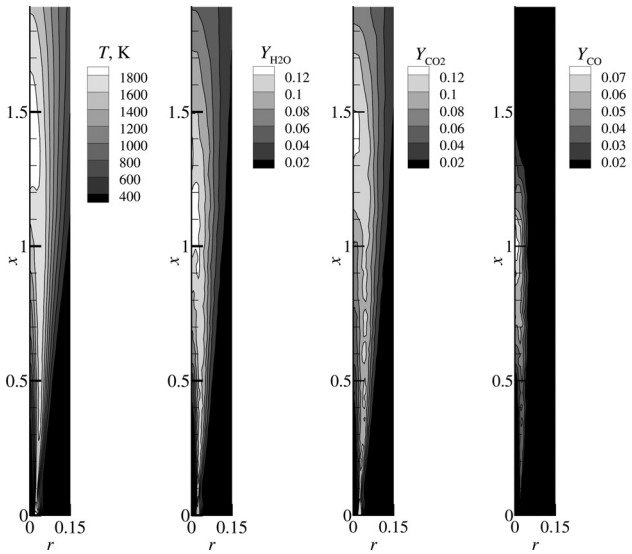

Fig. 7 Mean temperature and mass fraction fields for scaled Sandia Flame D

($R = 0.36$ m) and 95 cells along the axis ($z = 2.88$ m) with a square cuboid (Fig. 6) ($60 \times 60 \times 95$) at the center, and the cylinder walls are set to be black and cold. Figure 7 shows the temperature and concentration fields for the quasi-steady flame. The absorption coefficients of participating gases are nongray and are calculated using the full spectrum correlated-k (FSCK) model [19,20] requiring a set number of evaluations of the spectral RTE (corresponding to quadrature points in the FSCK scheme). In the present implementation, eight quadrature points are used.

The radiative heat source $-\nabla \cdot \mathbf{q}$ is shown in Fig. 8 for two axial locations. Location $z = 1.0$ m is where water vapor has the highest mass fraction, while the maximum mass fraction of carbon dioxide is at $z = 1.43$ m. The results calculated by P_1 to P_7 together with the FSCK spectral model on the cylindrical mesh are compared to line-by-line (LBL) P_1 calculations and LBL–PMC calculations. The error incurred by FSCK can be shown by comparing the FSCK–P_1 results with the LBL–P_1 results. And the LBL–PMC results presented here are calculated on a wedge mesh [21], which is another source of error. Still, major differences between the FSCK–P_N solutions and LBL–PMC results are errors attributable to the P_N methods. As shown in Fig. 8, with the increase of the order of P_N, the results get closer to the PMC results. And P_5 and P_7 successfully match the PMC results in most regions. The results prove that even under extremely alternating temperature fields and gas concentrations as in real combustion applications, the precision of the FSCK–P_5 and FSCK–P_7 are on the same level as LBL–PMC.

4.5 Computation Time Comparison. A CPU time comparison for different orders of P_N for the above cases is given in Table 1. All calculations were carried out on a single Intel (R) Xeon (R) CPU X7460 running at 2.66 GHz. The P_1 approximation solves a single PDE; P_3, P_5, and P_7 consist of 6, 15, and 28 strongly coupled PDEs with numerous cross-derivatives, respectively. The computing time for optically thick and intermediate cases does not show big differences. The optically thin case consumes more time because of the use of the boundary condition stabilizer. Comparing the computing time for the 3D cylindrical enclosures with the square enclosure, the time increase is not proportional to cell numbers. The cell number of the 3D cylindrical mesh is about 50 times of that of the square, but computing time is only around 12 times for P_1 and 40 times for P_5 to P_7, which implies that the computation time is strongly related to the distri-

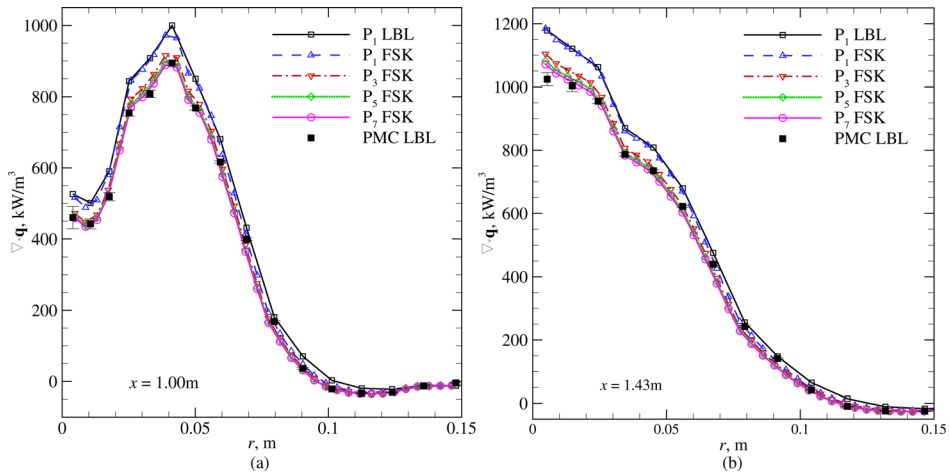

Fig. 8 Radiative source for Sandia Flame D × 4 at two axial locations as calculated with various P_N approximations. (*a*) $z = 1.00$ m and (*b*) $z = 1.43$ m.

Table 1 Comparison of P_N computation cost for different test cases

Computation cost of P_N method	Number of cells	P_1 (s)	P_3 (s)	P_5 (s)	P_7 (s)
Square enclosure ($C_k = 1$)	2601	0.02	0.75	4.71	7.00
Square enclosure ($C_k = 0.1$)	2601	0.02	0.87	5.05	9.33
Square enclosure ($C_k = 0.01$)	2601	0.02	1.78	7.09	19.19
3D cylinder	131,400	1.01	90.49	269.29	727.08
Flame (one quadrature)	957,600	7.36	1323.53	2566.52	6817.02

bution of radiative properties (through the number of iterations required). For radiative transfer evaluations in coupled CFD computations, the I_n^m results from the last iteration can be taken as initial values for the new iteration, which will significantly reduce the computation time of the P_N method; this is in contrast to DOM, which in the absence of scattering has to be evaluated from scratch at each time step.

5 Summary and Conclusion

A general spherical harmonics P_N model (up to P_7) for arbitrary 3D geometries is implemented in OPENFOAM. The coupled $N(N+1)/2$ simultaneous PDEs and their boundary conditions are solved iteratively by the PCG method. The implementation is tested for four example problems. Three problems are designed with smoothly varying radiative properties, and the fourth one is a real flame. Results from different orders of P_N for these cases are compared with exact solutions and PMC results. The comparison shows that high-order SHM can accurately predict the incident radiation and radiative heat source for a wide range of geometries and optical thicknesses. The answers get closer to the exact solution and PMC results with higher order P_N but with more PDEs to solve. The system of simultaneous PDEs is solved iteratively in the current implementation. Further development could employ a block-coupled approach [22] to improve the stability and computation efficiency.

Acknowledgment

Supported by National Science Foundation and the Department of Energy through Grant No. NSF1258635 is gratefully acknowledged.

Nomenclature

G = incident radiation (W m^{-2})
I = radiative intensity (W m^{-2} sr^{-1})
$\mathbf{I}$ = vector containing I_n^m
I_b = blackbody radiative intensity (W m^{-2} sr^{-1})
I_w = radiative intensity at wall (W m^{-2} sr^{-1})
I_n^m = position dependent radiative intensity coefficients
$\mathcal{L}$ = differential operator
N = order of the spherical harmonics method
$\hat{\mathbf{n}}$ = unit surface normal vector
$\mathbf{p}$ = coefficient vector for I_w
$\mathbf{q}_{(n,m)}$ = row vectors of the coefficient matrices
$\mathbf{Q}$ = coefficient matrices
r = radius (m)
$\mathbf{R}$ = rotation matrix
$\hat{\mathbf{s}}$ = unit direction vector
$\hat{\mathbf{t}}$ = unit surface tangential vector
Y_n^m = spherical harmonics
$\nabla \cdot \mathbf{q}$ = radiative heat source (W m^{-3})

Greek Symbols

α, β, γ = Euler rotation angles
β_r = extinction coefficient (m^{-1})
δ_{ij} = Kronecker delta function
$\Delta_{mm'}^n$ = rotation function
$\bar{\theta}$ = local polar angle
κ = absorption coefficient (m^{-1})
τ = optical coordinate, optical thickness
$\bar{\psi}$ = local azimuthal angle
ω = scattering albedo

Subscripts

j, k = indices for coefficient matrices and vectors
x, y, z = global coordinates
$\bar{x}, \bar{y}, \bar{z}$ = local coordinates

References

[1] Chandrasekhar, S., 1960, *Radiative Transfer*, Dover, New York.
[2] Lee, C. E., 1962, "The Discrete S_n Approximation to Transport Theory," Lawrence Livermore Laboratory, Technical Information Series Report No. LA2595.
[3] Chai, J. C., Lee, H. S., and Patankar, S. V., 1994, "Finite Volume Method for Radiation Heat Transfer," J. Thermophys. Heat Transfer, **8**(3), pp. 419–425.
[4] Howell, J. R., 1968, "Application of Monte Carlo to Heat Transfer Problems," *Advances in Heat Transfer*, Vol. 5, J. P. Hartnett and T. F. Irvine, eds., Academic, New York.
[5] Jeans, J. H., 1917, "The Equations of Radiative Transfer of Energy," Mon. Not. R. Astron. Soc., **78**(1), pp. 28–36.
[6] Chai, J. C., Lee, H. S., and Patankar, S. V., 1993, "Ray Effect and False Scattering in the Discrete Ordinates Method," Numer. Heat Transfer, Part B, **24**(4), pp. 373–389.
[7] Modest, M. F., 2013, *Radiative Heat Transfer*, 3rd ed., Academic, New York.
[8] Modest, M. F., and Yang, J., 2008, "Elliptic PDE Formulation and Boundary Conditions of the Spherical Harmonics Method of Arbitrary Order for General Three-Dimensional Geometries," J. Quant. Spectrosc. Radiat. Transfer, **109**(9), pp. 1641–1666.
[9] Yang, J., and Modest, M. F., 2007, "High-Order *P-N* Approximation for Radiative Transfer in Arbitrary Geometries," J. Quant. Spectrosc. Radiat. Transfer, **104**(2), pp. 217–227.
[10] Modest, M. F., 2012, "Further Developments of the Elliptic P_N-Approximation Formulation and Its Marshak Boundary Conditions," Numer. Heat Transfer, Part B, **62**(2–3), pp. 181–202.
[11] Jasak, H., Jemcov, A., and Tukovic, Z., 2007, "OpenFOAM: A C++ Library for Complex Physics Simulations," International Workshop on Coupled Methods in Numerical Dynamics, IUC, pp. 1–20.
[12] Marquez, R., and Modest, M. F., 2013, "Implementation of the PN-Approximation for Radiative Heat Transfer on OpenFOAM," ASME Paper No. HT2013-17556.
[13] Marshak, R. E., 1947, "Note on the Spherical Harmonics Method as Applied to the Milne Problem for a Sphere," Phys. Rev., **71**(7), pp. 443–446.
[14] Varshalovich, D. A., Moskalev, A. N., and Khersonskii, V. K., 1981, *Quantum Theory of Angular Momentum*, World Scientific, Singapore.
[15] Ravishankar, M., Mazumder, S., and Kumar, A., 2010, "Finite-Volume Formulation and Solution of the P_3 Equations of Radiative Transfer on Unstructured Meshes," ASME J. Heat Transfer, **132**(2), p. 023402.
[16] Nocedal, J., and Wright, S. J., 2006, *Numerical Optimization*, 2nd ed., Springer, Berlin.
[17] Press, W. H., 2007, *Numerical Recipes: The Art of Scientific Computing*, 3rd ed., Cambridge University, Cambridge, UK.
[18] Barlow, R. S., "International Workshop on Measurement and Computation of Turbulent Nonpremixed Flames (TNF)," http://www.sandia.gov/TNF/abstract.html
[19] Modest, M. F., 2003, "Narrow-Band and Full-Spectrum *k*-Distributions for Radiative Heat Transfer—Correlated-*k* vs. Scaling Approximation," J. Quant. Spectrosc. Radiat. Transfer, **76**(1), pp. 69–83.
[20] Modest, M. F., and Riazzi, R. J., 2005, "Assembly of Full-Spectrum *k*-Distributions From a Narrow-Band Database; Effects of Mixing Gases, Gases and Nongray Absorbing Particles, and Mixtures With Nongray Scatterers in Nongray Enclosures," J. Quant. Spectrosc. Radiat. Transfer, **90**(2), pp. 169–189.
[21] Wang, A., and Modest, M. F., 2007, "Spectral Monte Carlo Models for Nongray Radiation Analyses in Inhomogeneous Participating Media," Int. J. Heat Mass Transfer, **50**(19–20), pp. 3877–3889.
[22] Ferziger, J. H., and Perić, M., 2001, *Computational Methods for Fluid Dynamics*, 3rd ed., Springer, Berlin.